catalysts

MDPI

Article

Regulating Lattice Oxygen on the Surfaces of Porous Single-Crystalline NiO for Stabilized and Enhanced CO Oxidation

Xin Wen [1,2] and Kui Xie [2,3,*]

[1] College of Chemistry, Fuzhou University, Fuzhou 350108, China; wenxin@fjirsm.ac.cn
[2] Key Laboratory of Design and Assembly of Functional Nanostructures, Fujian Institute of Research on the Structure of Matter, Chinese Academy of Sciences, Fuzhou 350002, China
[3] Advanced Energy Science and Technology Guangdong Laboratory, Huizhou 116023, China
* Correspondence: kxie@fjirsm.ac.cn

Abstract: The long-range ordered lattice structure and interconnected porous microstructure of porous single crystals (PSCs) provide structural regularity and connectivity in remote electron movement to stabilize oxygen vacancies and activate lattice oxygen linked to surface active sites. In this work, we prepare NiO powder, single-crystal (SC) NiO, and PSC NiO. NiO contains a significant amount of oxygen vacancies. We find that the structure of porous NiO can create more oxygen vacancies. We load Pt onto these NiO crystals by atomic layer deposition (ALD) to activate lattice oxygen on definite NiO surfaces. The results show that Pt-loaded NiO effectively exhibits CO oxidation performance, in which Pt-loaded PSC NiO completely oxidizes CO at 65 °C. With 1% CO fully adsorbed, the density of activate lattice oxygen becomes an essential factor affecting performance. PSC NiO with deposited Pt clusters exhibited stable CO oxidation catalysis when run in air at ~65 °C for 300 h.

Keywords: porous single crystals (PSCs); NiO; oxygen vacancies; ALD; CO oxidation

Citation: Wen, X.; Xie, K. Regulating Lattice Oxygen on the Surfaces of Porous Single-Crystalline NiO for Stabilized and Enhanced CO Oxidation. *Catalysts* **2024**, *14*, 130. https://doi.org/10.3390/catal14020130

Academic Editor: Leonarda Liotta

Received: 9 January 2024
Revised: 31 January 2024
Accepted: 1 February 2024
Published: 7 February 2024

1. Introduction

Emissions from factories and exhaust fumes from fossil fuels contain large amounts of CO, which harms the human body and the atmosphere. Excess CO can affect atmospheric chemistry, poisoning the ozone layer and thus altering the climate. How to avoid CO pollution in the atmosphere is one of the most critical topics in treating the environment nowadays, and the design of highly active and stable loaded catalysts for the complete oxidation of CO is still a hot topic in academia and industry [1,2]. The transition elements have a single electron in their electronic configuration, and the complexes in this class have tunable valence electrons, electron densities, and an abundance of valence and valence electron configurations. Transition metal oxides are one of the most promising catalyst materials widely used in catalysis due to their unique activity and good stability [3,4]. For example, it has been shown that Au and NiO composite catalysts have high activity for CO oxidation reactions. The boundary density between a NiO patch and a Au surface can be maximized by proper redox pretreatment of a Au-NiO catalyst to achieve optimal activity. Preparing catalysts for ethane dehydrogenation by loading Nb onto NiO has also been studied. Nb fills cationic vacancies in the NiO lattice and substitutes for nickel atoms, and this substitution process likely results in a reduction in surface non-stoichiometric and cationic defects, which leads to a reduction in non-selective oxygen and thus an increase in ethane oxidative dehydrogenation (ODH) activity. These studies show that loaded catalysts have high potential with excellent catalytic performance. It can be understood that NiO is a typical fully oxidized catalyst with outstanding performance in fully oxidized catalytic reactions [5–8].

NiO is a transition metal oxide and a p-type semiconductor. The bulk phase of NiO is a face-centered cubic structure, and each Ni atom (or O atom) in the lattice is

connected to six O atoms (or Ni atoms), respectively, in a six-coordinated state. NiO is a non-stoichiometric oxide with cationic vacancies that can accommodate a significant excess of electrophilic oxygen radicals and is a solid oxidizing substance [7,9–11]. The structural defects present in NiO result in many vacancies, which lead to the formation of strongly oxidizing electrophilic oxygen, and NiO exhibits superior oxidative properties in catalytic reactions [12,13]. The surface of NiO is rich in hydroxyl groups, and these hydroxyl groups will actively participate in catalytic reactions to reduce the catalytic temperature and improve catalytic efficiency. NiO is widely available and inexpensive, so we can design an efficient catalyst for CO oxidation based on NiO [14–17].

A single-crystalline substance is one in which the particles within the substance are spatially, regularly, and periodically arranged. Construction of catalytically active sites on the surface of a material needs to be based on the structure of the material. Polycrystalline and amorphous materials have complex surface structures, while single-crystalline structures are long-range ordered. Single-crystalline regular periodic arrays provide a unique advantage for precisely creating active sites on catalytically active surfaces [18–20]. Porosity is the presence of directional or random pores within a material. A material's specific surface area increases due to its porous structure, exposing more active sites.

PSC materials have the properties of both single-crystalline and porous structures. PSCs are widely used in various fields: TiO_2, SnO_2, Cr_2O_3, ZrO_2, and other PSC materials are used in the field of semiconductors and PSC TiO_2, CeO_2, and $SrTiO_3$ are applied in the field of catalysis [21–26]. PSCs combined with an ordered lattice structure and disordered interconnected pores will produce a well-defined surface structure, with the single-crystalline nature of the monomer providing high stability similar to that of bulk single-crystalline materials and the porous nature of the monomer providing higher catalytic activity identical to that of nanocrystals. The pore structure of PSCs dramatically increases the specific surface area of a material, thus increasing the number of active sites and the rate of reaction by increasing the number of electron transport channels between the catalyst and the reactants. Due to the single-crystalline nature of PSCs, a single-crystalline skeleton has no grain boundaries, and fast electron transfer can be achieved by reducing electron scattering in a porous structure. PSCs exhibit a well-defined lattice structure, precise chemical composition, and clear termination surfaces, while maintaining both high stability and activity [27–29]. Therefore, it is crucial to study PSCs as catalytic substrates.

In the present study, we consider constructing stable, efficient, and affordable loaded catalysts for CO oxidation by loading Pt onto PSC NiO and modulating surface oxygen defects [30–32]. The potential applications of porous metal oxide materials are evaluated, providing a valuable reference for future studies.

2. Results

XRD is used to analyze crystal structure, while SEM is used for surface morphology observation. Figure 1 shows XRD and SEM images of precursor single-crystalline Ni $(HCO_3)_2$ and PSC NiO. Raman spectra of Ni $(HCO_3)_2$ precursor with PSC NiO are displayed in Figure S1. Figure 1a shows the XRD pattern and crystal ball-and-stick structure model of a Ni $(HCO_3)_2$ single-crystalline sample. The diffraction peaks of the Ni $(HCO_3)_2$ precursor overlap with those of PDF#150782, and the high signal of peak intensity proves that Ni $(HCO_3)_2$ crystals have been synthesized successfully and have better crystal characteristics. Figure 1c,e shows the XRD spectrum and crystal ball-and-stick structure model of SC NiO and PSC NiO. The diffraction peaks of NiO coincide with those of PDF#711179, which belongs to the cubic system. Figure S2 presents XRD Rietveld refinement patterns of the samples.

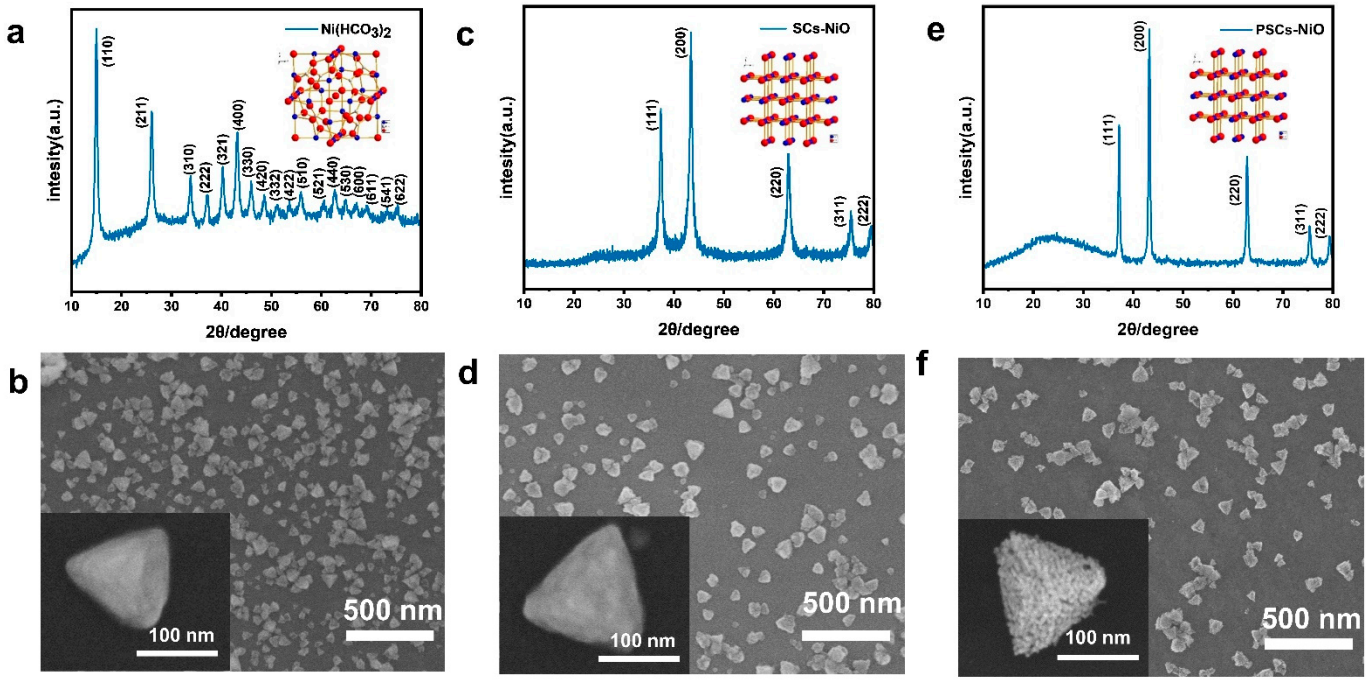

Figure 1. (**a**) XRD patterns of Ni $(HCO_3)_2$ single-crystalline sample, with the structure of Ni $(HCO_3)_2$ single crystals in the inset. (**b**) SEM image of Ni $(HCO_3)_2$ single-crystalline sample. (**c**) XRD patterns of SC NiO, with the structure of NiO single crystals in the inset. (**d**) SEM image of SC NiO. (**e**) XRD patterns of PSC NiO, with the structure of NiO single crystals in the inset. (**f**) SEM image of PSC NiO. (An SEM image of a single particle is shown in the lower left corner of the image.).

Figure 1b shows an SEM image of Ni $(HCO_3)_2$, which can be observed as a non-porous tetrahedral shape. Ni $(HCO_3)_2$ grain size is between 100 and 300 nm, and porous NiO nanoparticles obtained from Ni $(HCO_3)_2$ precursor have the same size as those of Ni $(HCO_3)_2$, both of which are tetrahedral in morphology. SC NiO has smooth surfaces in Figure 1d, but the surfaces of PSC NiO are not as smooth in Figure 1f. The reason for this difference is the formation of worm-like pores in PSC NiO. The conversion of Ni $(HCO_3)_2$ into the crystal structure of NiO remains stable without structural collapse or shrinkage. Figure S3 shows the weight change in the process of single-crystalline Ni $(HCO_3)_2$ into PSC NiO and the schematic process of crystal structure modeling. Figure S3a exemplifies the weight change during the conversion of Ni $(HCO_3)_2$ to NiO. The TG curve shows that there is a mass loss of 43.27%, which is less than the theoretical value (57.0%) for the decomposition of Ni $(HCO_3)_2$ to produce NiO, which may be since a portion of the precursor has been converted to NiO during the process of growing the Ni $(HCO_3)_2$ precursor. Figure S3b demonstrates the schematic process of the modeled crystal structure for transforming Ni $(HCO_3)_2$ to NiO.

In order to analyze the microstructure and crystal orientation of the NiO used in PSCs, crystals were characterized by TEM and HR-TEM. It can be observed from Figure 2a,d,g that the crystal size ranges between 100 and 300 nm, which is consistent with SEM observations. A comparison of the three images shows an apparent porous structure in Figure 2g. The crystal spacing of Ni $(HCO_3)_2$ and NiO can be observed very clearly in Figure 2b,e,h. The precise lattice spacing indicates that Ni $(HCO_3)_2$ and NiO have excellent crystallinity. The crystal face spacings of Ni $(HCO_3)_2$ and NiO are 0.618 nm and 0.237 nm, corresponding to the (511) face of Ni $(HCO_3)_2$, the (111) face of SC NiO, and the (111) face of PSC NiO, respectively. Figure 2c,f,i shows SAED maps of Ni $(HCO_3)_2$, SC NiO, and PSC NiO, and it can be seen that all are single-crystal diffractions. These images show that Ni $(HCO_3)_2$ and NiO maintain good single-crystalline properties, and even though NiO has a porous structure, the samples remain single-crystalline like the precursor.

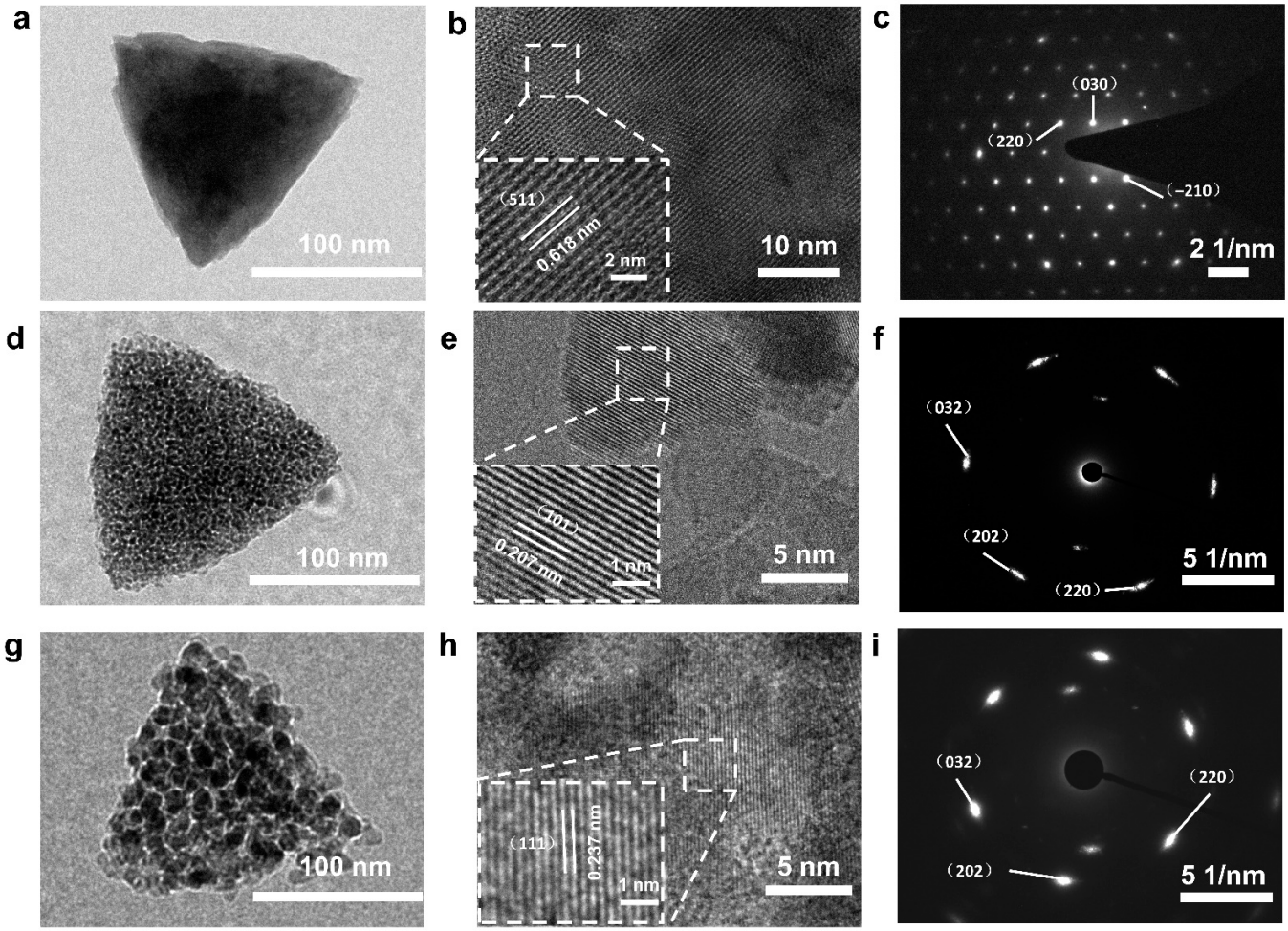

Figure 2. TEM images, HRTEM images, and SAED patterns of Ni $(HCO_3)_2$ precursor (**a**–**c**), SC NiO (**d**–**f**), and PSC NiO (**g**–**i**). (The lower left corner pictures of (**b**,**e**,**h**) in the figure are partial enlarged images.).

Differences in the oxygen vacancies contained in NiO with different morphologies were compared by a series of characterizations. To analyze the metal oxidation state, XPS characterization of NiO was performed. The XPS spectra in Figure 3a show the difference in the spectra of catalysts with different morphologies, lattice oxygen, oxygen vacancies, and surface adsorbed oxygen by integrating the area of each spectrum. The peak at 529.4 eV is attributed to lattice oxygen (O_a: O^-); the peak at 531.3 eV is attributed to surface oxygen (O_b: O^{2-}, O_2^{2-}, or O^-); and the peaks above 532.0 eV are attributed to other weakly bound oxygen species (O_g) such as carbonate (CO_3^{2-}), adsorbed molecular water, and hydroxyl groups (OH^-). The density of oxygen vacancies (O_v) can be considered as $O_b/(O_a + O_b + O_g)$. We find that the densities of oxygen vacancies (O_v) in NiO are as follows: PSC NiO (0.26) > SC NiO (0.21) > powder NiO (0.16), which is consistent with the results in Figure 3b [33–35]. We discover a significant number of O_v in NiO, and we use platinum to further modulate these vacancies. To investigate the performance of a complete oxidation reaction with CO, Figure S4a shows high-sensitivity low-energy ion scattering spectra (HS-LEIS) of PSC NiO, confirming the atomic termination layer of Ni and O on the surface. Figure 3c shows the HS-LEIS spectra of PSC NiO loaded with Pt; its surface elements add Pt [36,37]. Figure S5 shows the XPS spectra of the integral spectrum, C 1s peaks, and Ni 2p peaks of PSC NiO, SC NiO, and powder NiO; the experimental results are consistent with the theoretical predictions, indicating accurate preparation of PSC NiO, SC NiO, and powder NiO. The Pt 4f spectrum of PSC NiO loaded with Pt contains two peaks corresponding to Pt $4f_{5/2}$ and Pt $4f_{7/2}$, which indicate that platinum exists in metal

and ionic form (Figure 3d). The as-received sample contains Pt^0 and Pt^{2+} states in 56.32% and 43.68%. In Figure 3e, Ni, O, and Pt are evenly spread across the surface of PSC NiO.

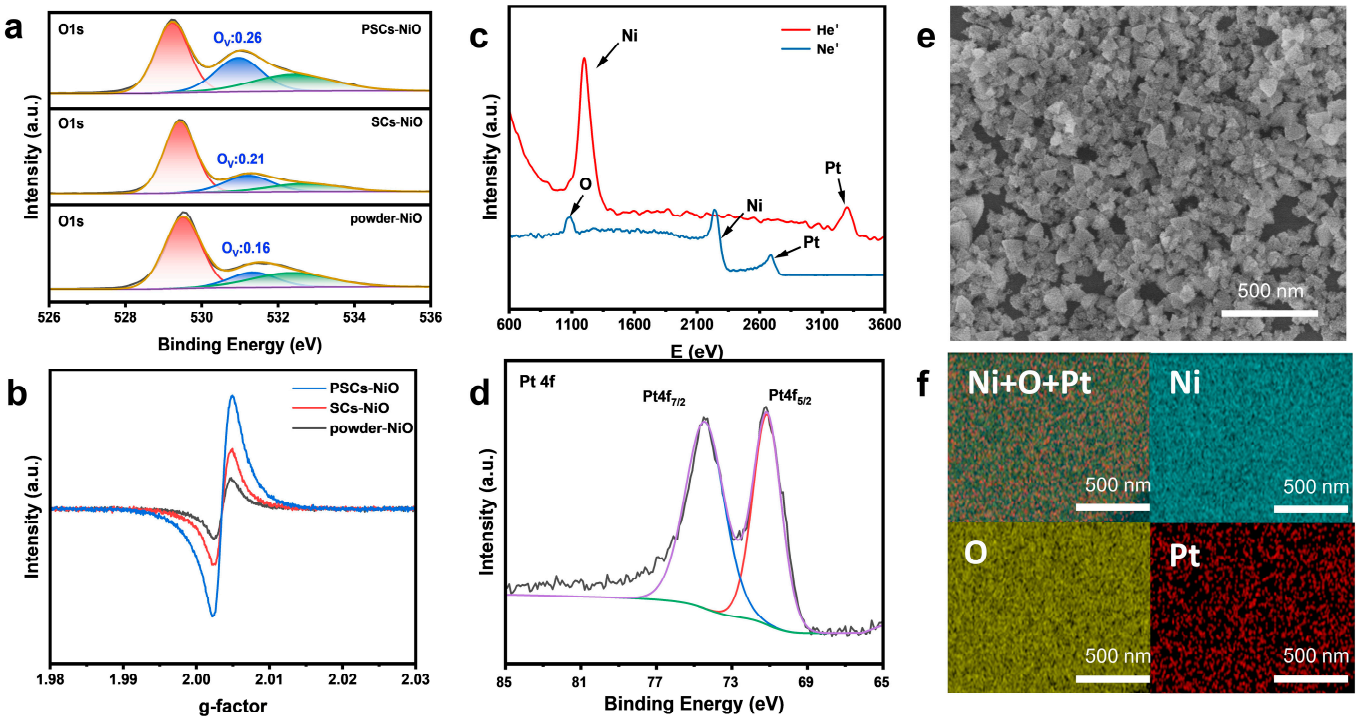

Figure 3. (**a**) XPS spectra of the O 1s peaks of powder NiO, SC NiO, and PSC NiO. (**b**) EPR spectra of powder NiO, SC NiO, and PSC NiO. (**c**) HS-LEIS spectra of NiO loaded with Pt. (**d**) XPS spectra of the Pt 4f peaks of NiO loaded with Pt. (**e**,**f**) EDS elemental mapping of NiO loaded with Pt.

In Figure S6a, the presence of Pt dramatically alters PSC NiO reducibility, resulting in a shift of both characteristic TPR peaks to a lower temperature. The enhancing effect of Pt on NiO reduction towards metallic nickel indicates that Pt favors the formation of PSC NiO oxygen vacancies. The EXAFS are also characterized by a change in oxygen vacancies between loaded and unloaded on the catalyst surface, as shown in Figure S6b. The region around 533 eV is assigned to the oxygen p character of the transition metal 3d band, and the broader structures at 537 eV and 540 eV belong to the oxygen p part of the metal 4s and 4p bands, respectively. After loading Pt, the O K-edge peak position is shifted to the right, the electronic excited state energy of oxygen becomes higher, and the oxygen activity increases more easily to form PSC NiO oxygen vacancies [38–41]. The results of the Pt nanoparticle size distribution are displayed in Figure S7a, which range from 1.1 to 1.9 nm, with an average size of only 1.48 nm, belonging to the category of nanoclusters (<2 nm). Figure S7b–f shows a mapping image of PSC NiO with 2.07 wt% Pt sample, in which it can be clearly seen that the Pt nanoclusters are uniformly dispersed on the surface.

Figure 4a,b shows in situ FT-IR of CO with air at the Pt/NiO sites in PSC NiO. The adsorption strength of CO gradually increases with increasing temperature, and there is a strong affinity for CO at the Pt/NiO active site. The stretching vibrations of C=O in CO_2 become progressively stronger above an onset temperature of 30 °C. Higher operating temperatures accelerate CO oxidation by activating lattice oxygens connected to surface Pt. In situ FT-IR analysis investigated the surface-adsorbed substances for CO oxidation during the catalytic process. During the reaction, hydroxyl groups on the catalyst surface tend to form carboxyl groups with CO. In Figure 4d, the broad band around 1390 cm^{-1} could be assigned to bicarbonates. The broad band around 1363 cm^{-1} could be assigned to formate. The broad band around 1334 cm^{-1} could be assigned to monodentate carbonate. The broad band around 1278 cm^{-1} could be assigned to bidentate carbonates [42]. Figure 4e shows

the in situ FT-IR of CO adsorption on Pt clusters on PSC NiO. The narrow band around 2060 cm^{-2} can be reasonably attributed to the linear adsorption of CO at the Pt site, the intensity of which decreased when we flowed He for desorption. Pt clusters on PSC NiO have an extreme affinity for CO, and the higher the active site density, the more muscular the adsorption strength. The efficient activation of CO oxidation by lattice oxygen in the interfacial structure is indicated by the disappearance of the adsorption strength of CO when flowing O_2 undergoes desorption.

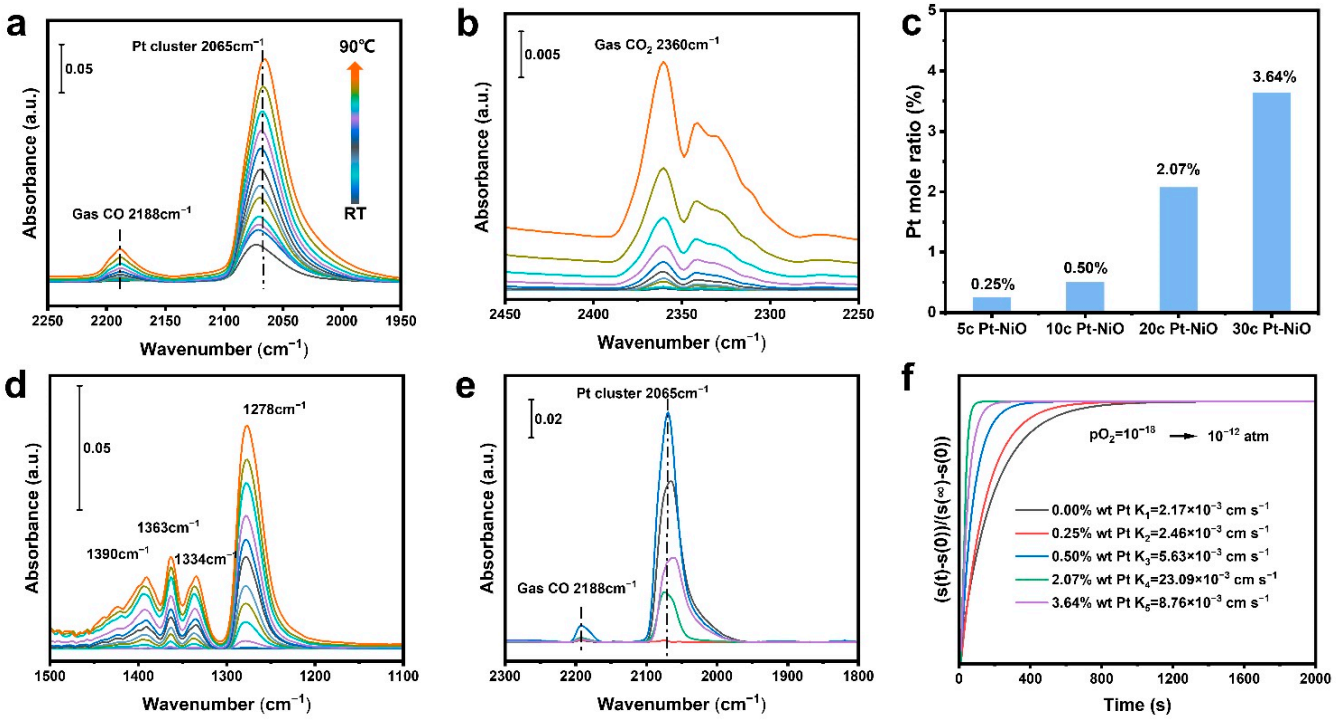

Figure 4. (**a**,**b**,**d**) In situ FT-IR of CO oxidation with air using PSC NiO with 2.07 wt% Pt. (**e**) In situ FT-IR of CO adsorption at the Pt/NiO sites in PSC NiO with 2.07 wt% Pt loading contents. Blue lines indicate CO adsorption after equilibrium with CO; black color indicates CO adsorption after moving to He for 2 min; and purple, green, and red lines indicate CO adsorption after moving to O_2 for 2 min, 4 min, and 8 min, respectively. (**c**) The loading content of Pt in PSC NiO. (**f**) Surface oxygen exchange coefficients of PSC NiO with different Pt loadings.

The actual amounts of loaded Pt are 0 wt%, 0.25 wt%, 0.50 wt%, 2.07 wt%, and 3.64 wt% for 5, 10, 20, and 30 cycles on NiO substrate, respectively, as shown in Figure 4c. Figure 4f illustrates the surface oxygen exchange coefficient (K_{ex}) of NiO, which demonstrates the rapid equilibrium of the surface defect reaction $O_{O^x} + 2h\cdot \leftrightharpoons VO\cdot\cdot + 1/2O_2$. This indicates that the presence of oxygen deficiency increases the surface oxygen exchange coefficient by approximately 10 times.

The catalyst performance was investigated by GC, and the complete reaction temperature was tested as a measure of catalyst performance. Figure 5a illustrates the CO oxidation process, where the catalyst completely oxidized CO at 240 °C, 205 °C, and 175 °C for commercial powder NiO, SC NiO, and PSC NiO, respectively. Figure 5b shows that the performance of NiO was enhanced substantially after loading Pt. PSC NiO loaded with 0.25% Pt could completely oxidize CO at 160 °C, and the temperature of complete oxidation decreased with increasing content until it started to have a side effect on the catalytic reaction. The experimental results show that loading of 2.07% has the most robust catalytic performance and can be fully converted at 65 °C. Beyond this loading, the temperature of complete oxidation will increase. Figure 5d shows the long-term stability test results of PSC NiO with loaded Pt and that 0.25 wt% Pt/PSC NiO, 0.50 wt% Pt/PSC NiO, and 2.07 wt%

Pt/PSC NiO were able to maintain the long-term stability of 300 h without decay. The stability of the catalyst is further demonstrated by the approximately identical dynamics of the catalyst at 70~300 h CO oxidation, as shown in Figure 5e [43–45].

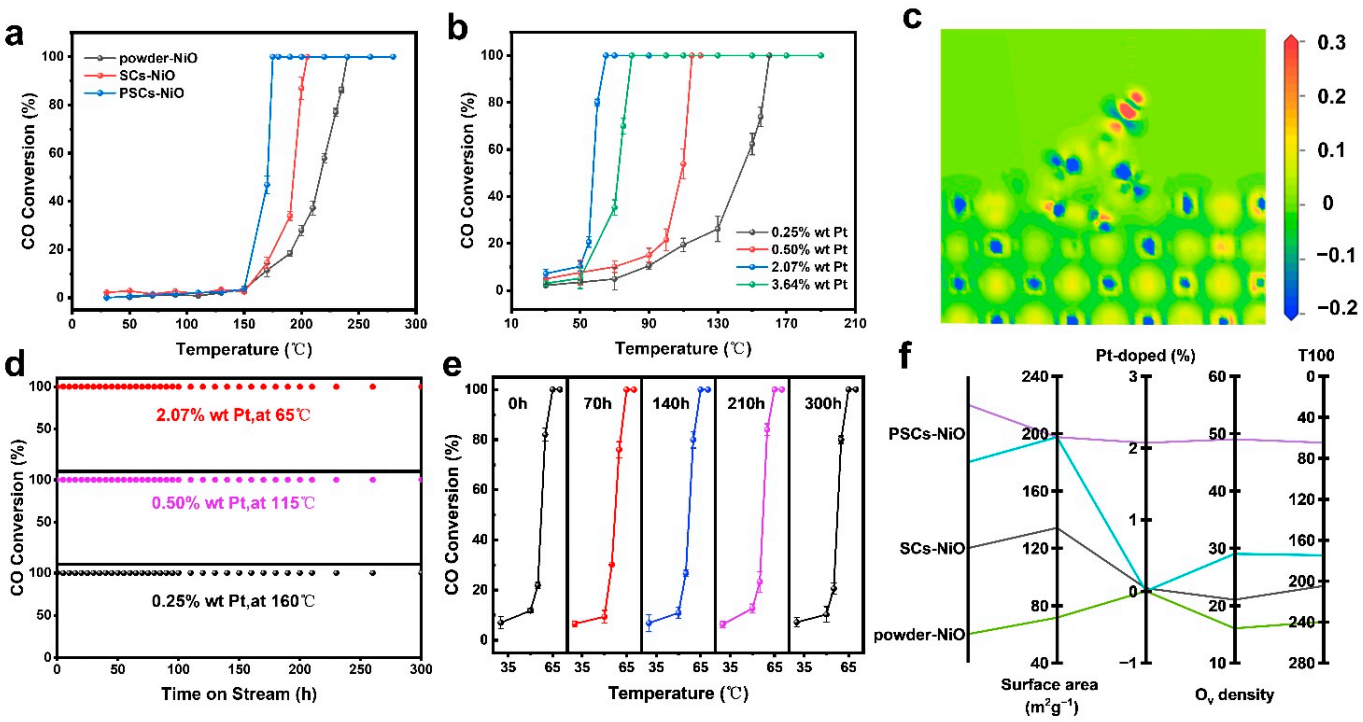

Figure 5. (**a**) CO oxidation properties of NiO commercial powders, SC NiO, and PSC NiO without Pt. (**b**) CO oxidation properties of 0.25 wt%, 0.50 wt%, 2.07 wt%, and 3.64 wt% Pt loaded onto PSC NiO. (**c**) Activation and electron transfer of PSC NiO in CO oxidation. (**d**) CO oxidation properties of PSC NiO with different Pt loadings at 65 °C, 115 °C, and 160 °C. (**e**) CO oxidation kinetics of PSC NiO containing 2.07 wt% Pt at 70~300 h. (**f**) Correlation of NiO morphology, surface area, Pt doping, and O_v density content with CO complete oxidation temperature.

The Mars-van-Krevelen mechanism is generally followed in catalysts with reducible carriers. Activated CO directly reacts with the interfacial lattice oxygen of the reducible page to produce oxygen vacancies. Subsequently, gas-phase oxygen adsorbs oxygen vacancies and continues to participate in the reaction after being activated by the electron-rich environment created by the oxygen vacancies, with the noble metal or loaded reactive metal providing the CO adsorption sites. The results of the adsorption activation process of CO molecules on the surface of PSC NiO obtained by DFT calculations are shown in Figure 5c. The red region gains electrons and the blue region loses electrons. The darker the red color (the larger the value), the more electrons are gained, and the darker the blue color (the larger the value), the more electrons are lost. It can be seen that CO loses electrons on Pt to form CO^{2+} and oxygen forms O^{2-} on PSC NiO to participate in the reaction, which is consistent with the Mars-van-Krevelen mechanism.

Figure S8a–c shows the N_2 adsorption and desorption isotherms for NiO powder, SC NiO, and PSC NiO, respectively. The BET-specific surface areas (Figure S8d) of NiO powder, SC NiO, and PSC NiO are about 71.4640 $m^2\ g^{-1}$, 134.1370 $m^2\ g^{-1}$, and 197.4990 $m^2\ g^{-1}$, respectively. Meanwhile, the average pore sizes of PSC NiO nanoparticles are ~15 nm and can be characterized by BET. The pores shown in Figure 1 and Figure S9 confirm the pore size from BET. Figure 5f displays the temperature of full CO oxidation catalyzed by powder NiO, PSC NiO, and SC NiO with different loadings. From Figure 5f, it can be observed that PSC NiO outperforms SCs, and SCs outperform powder. With an increase in Pt loading onto PSC NiO, the complete oxidation temperature decreases. When the

complete oxidation temperature reaches its lowest at one loading, the performance no longer increases but decreases. It can be concluded that single-crystalline NiO outperforms amorphous NiO, with enhanced performance as the specific surface area becomes more extensive and as the loading increases.

The stability of a catalyst is an essential part of a catalyst's performance, and the ability of a catalyst to maintain its structure and morphology after a reaction dramatically determines whether the catalyst can be used for an extended period. Figure 6a,b shows the XRD and Raman spectra after the reaction, showing that the crystal structure of PSC NiO did not change after the catalytic reaction and still maintained good crystallinity. Figure 6c,d shows the SEM and TEM of the catalyst after the reaction, and it can be observed that connected pores in the catalyst still existed and had a precise shape without collapse or deformation. Figure 6e,f shows the lattice fringes of the catalyst with SAED, both consistent with the pre-reaction. The results show that Pt-modified PSC NiO is very stable in the catalytic reaction of CO oxidation and has the potential to work effectively for a long time. A comparison of the performance of some loaded catalysts for the reaction of complete oxidation of CO is shown in Table S1.

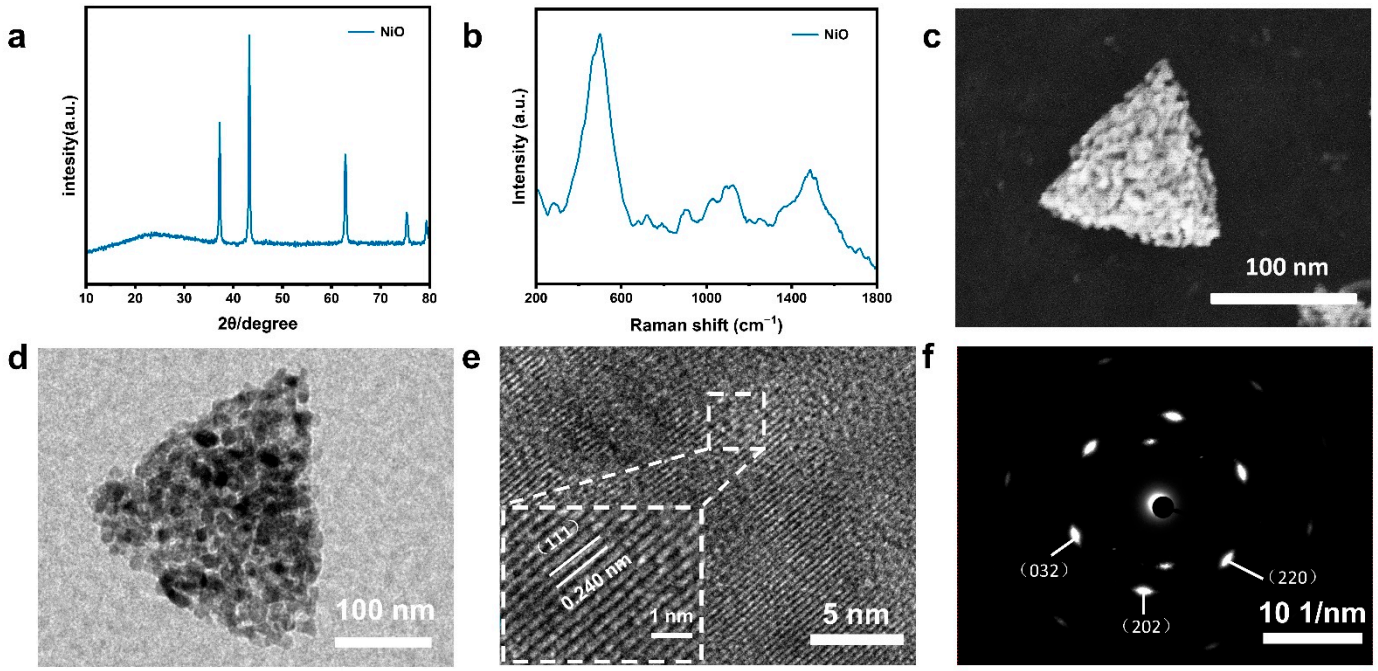

Figure 6. (**a**) XRD of the reacted PSC NiO. (**b**) Raman spectra of the reacted PSC NiO. (**c**) SEM images of the reacted PSC NiO (SEM images of individual particles are shown in the lower left corner of the images). (**d**–**f**) FETEM images, HRTEM images, and SAED plots of the reacted PSC NiO.

3. Experiments

3.1. Syntheses of Porous Pt/NiO Crystals

SC Ni $(HCO_3)_2$ was grown by the hydrothermal method. All reagents were analytical grade and did not require further purification. To create a clear green solution, a mixture of 0.640 g $NiCl_2 \cdot 6H_2O$, 1.480 g urea, and 1.480 g PVP K30 was dissolved in 66.4 mL ethylene glycol (EG) and 5.6 mL distilled water. This was conducted with vigorous stirring for three hours. The solution was transferred to a 100 mL Poly tetra fluoro ethylene (PTFE) lined autoclave, sealed, heated to 160 °C, kept for 12 h, and cooled to ambient temperature. A green Ni $(HCO_3)_2$ precipitate was obtained. The precipitate was collected through centrifugation, washed with ethanol-deionized water several times, and dried at room temperature. The green Ni $(HCO_3)_2$ precipitate was calcined in a muffle furnace at 300 °C and 400 °C for two hours at an elevated rate of 5 °C min^{-1} to obtain NiO. In the following,

the samples obtained by calcination at 300 °C and 400 °C are named N300 and N400, respectively. A growth schematic is shown in Figure S10.

Atomically dispersed platinum was confined to the surface of PSC NiO using ALD. (Trimethyl)methylcyclopentadienyl platinum (IV) and O_3 were precursors, and ultra-high-purity Ar (99.999%) was used as the carrier gas at a flow rate of 50 mL min^{-1}. The (Trimethyl)methylcyclopentadienyl platinum (IV) precursor vial was heated to 70 °C for sufficient vapor pressure. The ALD chamber was heated to 300 °C, and the precursor inlet tube was kept at 150 °C. When the temperature of each part reached the set temperature and was maintained for a certain period, 100 mg of carrier was loaded into the ALD reaction chamber. The precursor (Trimethyl)methylcyclopentadienyl platinum (IV) pulse time, Ar gas purge time, O_3 pulse time, and Ar gas purge time were 60 s, 30 s, 30 s, and 30 s, in that order, which was one cycle of Pt ALD.

3.2. Characterization

Phase characterization was analyzed by X-ray diffraction (XRD, Mini-Flex 600; Rigaku, Tokyo, Japan), and the formation and orientation of the crystal planes were determined. The morphology, pore distribution, and size of NiO crystals at an accelerating voltage of 5.0 kV were observed using field emission scanning electron microscopy (FE-SEM, SU8010; Hitachi, Tokyo, Japan). The orientation of the sample lattice was characterized by transmission electron microscopy (TEM, JEOL JEM-F200; JEOL, Tokyo, Japan) at 200 kV. EPR spectra were recorded on a spectrometer (Bruker Biospin GMBH E500 10/12; Bruker, Ettlingen, Germany) to determine oxygen vacancies. Valence was detected by X-ray photoelectron spectroscopy (XPS, ESCALAB 250Xi, Waltham, MA, USA). The surface area of BET was tested using automated surface and microporous analysis (Tristar II 3020; Micromeritics, Norcross, GA, USA). The concentration of Ni and Pt was measured with an Ultima-2 ICP-OES machine (Horiba, Paris, France). Diffuse Reflectance Infrared Fourier Transform Spectroscopy (DRIFTS) tests were performed by an infrared spectrometer (Bruker VERTEX 70; Bruker, Ettlingen, Germany). A single test was performed using 100 mg of 2.07 wt% Pt PSC NiO, and the test temperature was gradually increased from room temperature to 90 °C (data were collected every 5 °C). The reaction gas comprised 1% CO, and the equilibrium gas was air. The reaction gas was flowed through the reactor at a rate of 50 sccm. Raman spectral data were obtained using a Raman spectrometer (LabRAMHR, Horiba J. y; Horiba, Paris, France) equipped with a 50× high-magnification objective.

3.3. Oxidation Reaction

The CO catalyzed reaction was carried out at atmospheric pressure in a tubular quartz reactor with an inner diameter of 5 mm. A single test was performed using 100 mg of catalyst, and the test temperature was gradually increased from 30 °C to 300 °C. The test was performed at a rate of 3 °C min^{-1}. The rate of temperature increase was 3 °C min^{-1}, and a set of data was collected at 20 °C intervals. The reaction gas comprised 1% CO, and the equilibrium gas was air. The reaction gas was flowed through the reactor at a rate of 50 sccm. The tail gas was then connected to a gas chromatograph (GC) for on-line analysis. The GC system used was equipped with a flame ionization detector (FID) and a thermal conductivity detector (TCD) (GC-2014; Shimadzu, Kyoto, Japan).

4. Conclusions

In summary, we grew nano tetrahedral NiO single-crystalline samples with good crystallinity and morphology and prepared PSC NiO loaded with Pt by ALD. NiO is a typical transition metal complex that has adjustable valence electrons, electron densities, and a rich variety of valence and valence electron configurations and contains a significant amount of oxygen vacancies. To construct highly active surfaces, we utilized an ultra-high specific surface area with the advantages of structural regularity and good connectivity for remote electron movement in the PSCs to create more oxygen vacancies. Platinum-loaded nanoparticles activated lattice oxygen in PSC NiO; the proportion of Ov on the

surface was a critical factor in determining the performance of the reaction. We found that platinum-modified PSC NiO was able to fully oxidize CO at 65 °C, with no performance degradation even after 300 h of continuous operation. This provides important value for the design and application of other metal-based materials. This work proposes new strategies for designing metal-based materials and provides a reference for future research on inexpensive CO complete oxidation catalysts.

Supplementary Materials: The following supporting information can be downloaded at: https://www.mdpi.com/article/10.3390/catal14020130/s1, Figure S1. (a) Raman spectra of PSCs NiO. (b) Raman spectra of Ni $(HCO_3)_2$ precursor, Figure S2. XRD Rietveld refinement patterns of (a) Ni $(HCO_3)_2$; (b) NiO, Figure S3. (a) Thermogravimetric curves of the transformation of Ni $(HCO_3)_2$ precursor to NiO. (b) Schematic of the crystal structure model for the transformation of Ni $(HCO_3)_2$ to NiO, Figure S4. (a) HS-LEIS spectra of PSC NiO, Figure S5. The integral XPS spectrum (a, d, g); XPS spectra of the C 1s (b, e, h); XPS spectra of the Ni 2p peaks of PSC NiO, SC NiO and powder NiO (c, f, i). (a - c) PSC NiO; (d - f) SC NiO; (g – i) powder NiO, Figure S6. (a) H_2-TPR profiles of NiO and Pt/NiO. (b) EXAFS of NiO and Pt/NiO oxygen atoms in the lattice, Figure S7. (a) Cs-HAADF-STEM images of PSC NiO with 2.07 wt% Pt, and (b-f) the mapping of PSC NiO with 2.07 wt% Pt, Figure S8. (a-c) N_2 adsorption desorption isotherms of (a) NiO powder, (b) NiO SCs, (c) NiO PSCs. (d) BET-specific surface areas of powder NiO, SC NiO, and PSC NiO, Figure S9. (a) Pore size statistics of TEM images from PSC NiO, Figure S10. Preparation of PSC NiO precursors by hydrothermal method, Table S1. Comparison of catalysts for the complete oxidation of CO. References [46–54] are cited in the supplementary materials.

Author Contributions: Conceptualization, X.W.; methodology, K.X.; software, X.W.; validation, X.W.; formal analysis, X.W.; investigation, K.X.; resources, K.X.; data curation, X.W.; writing—original draft preparation, X.W.; writing—review and editing, X.W.; visualization, X.W.; supervision, X.W.; project administration, K.X.; funding acquisition, K.X. All authors have made a substantial, direct, and intellectual contribution to the work and approved it for publication. All authors have read and agreed to the published version of the manuscript.

Funding: This work was supported by the Natural Science Foundation of China (22325506), and Fujian STS plan supporting project (2022T3022, 2023T3050, and 2023T3051).

Data Availability Statement: The data supporting the findings of this study are available from the corresponding authors K.X. (kxie@fjirsm.ac.cn) upon reasonable request.

Conflicts of Interest: The authors declare no conflict of interest.

References

1. Peng, G.; Merte, L.R.; Knudsen, J.; Vang, R.T.; Laegsgaard, E.; Besenbacher, F.; Mavrikakis, M. On the Mechanism of Low-Temperature CO Oxidation on Ni(111) and NiO(111) Surfaces. *J. Phys. Chem. C* **2010**, *114*, 21579–21584. [CrossRef]
2. Liu, W.; Tang, K.; Lin, M.; June, L.T.O.; Bai, S.-Q.; Young, D.J.; Li, X.; Yang, Y.-Z.; Hor, T.S.A. Multicomponent (Ce, Cu, Ni) oxides with cage and core–shell structures: Tunable fabrication and enhanced CO oxidation activity. *Nanoscale* **2016**, *8*, 9521–9526. [CrossRef] [PubMed]
3. Han, S.W.; Kim, D.H.; Jeong, M.-G.; Park, K.J.; Kim, Y.D. CO oxidation catalyzed by NiO supported on mesoporous Al_2O_3 at room temperature. *Chem. Eng. J.* **2016**, *283*, 992–998. [CrossRef]
4. Jeong, M.-G.; Kim, I.H.; Han, S.W.; Kim, D.H.; Kim, Y.D. Room temperature CO oxidation catalyzed by NiO particles on mesoporous SiO_2 prepared via atomic layer deposition: Influence of pre-annealing temperature on catalytic activity. *J. Mol. Catal. A Chem.* **2016**, *414*, 87–93. [CrossRef]
5. Xu, X.; Fu, Q.; Guo, X.; Bao, X. A Highly Active "NiO-on-Au" Surface Architecture for CO Oxidation. *ACS Catal.* **2013**, *3*, 1810–1818. [CrossRef]
6. Zhu, H.; Ould-Chikh, S.; Anjum, D.H.; Sun, M.; Biausque, G.; Basset, J.-M.; Caps, V. Nb effect in the nickel oxide-catalyzed low-temperature oxidative dehydrogenation of ethane. *J. Catal.* **2012**, *285*, 292–303. [CrossRef]
7. Heracleous, E.; Lemonidou, A. Ni–Nb–O mixed oxides as highly active and selective catalysts for ethene production via ethane oxidative dehydrogenation. Part I: Characterization and catalytic performance. *J. Catal.* **2006**, *237*, 162–174. [CrossRef]
8. Heracleous, E.; Lemonidou, A. Ni–Nb–O mixed oxides as highly active and selective catalysts for ethene production via ethane oxidative dehydrogenation. Part II: Mechanistic aspects and kinetic modeling. *J. Catal.* **2006**, *237*, 175–189. [CrossRef]
9. Antolini, E. $Li_xNi_{1-x}O$ ($0<x\leq0.3$) solid solutions: Formation, structure and transport properties. *Mater. Chem. Phys.* **2003**, *82*, 937–948. [CrossRef]

10. Atanasov, M.; Reinen, D. Non-local electronic effects in core-level photoemission, UV and optical electronic absorption spectra of nickel oxides. *J. Electron Spectrosc. Relat. Phenom.* **1997**, *86*, 185–199. [CrossRef]
11. Al Soubaihi, R.; Saoud, K.; Dutta, J. Critical Review of Low-Temperature CO Oxidation and Hysteresis Phenomenon on Heterogeneous Catalysts. *Catalysts* **2018**, *8*, 660. [CrossRef]
12. Deraz, N.M.; Selim, M.M.; Ramadan, M. Processing and properties of nanocrystalline Ni and NiO catalysts. *Mater. Chem. Phys.* **2009**, *113*, 269–275. [CrossRef]
13. Bhardwaj, N.; Singh, A.K.; Tripathi, N.; Goel, B.; Indra, A.; Jain, S.K. Ni–NiO heterojunctions: A versatile nanocatalyst for regioselective halogenation and oxidative esterification of aromatics. *New J. Chem.* **2021**, *45*, 14177–14183. [CrossRef]
14. Park, E.J.; Lee, J.H.; Kim, K.-D.; Kim, D.H.; Jeong, M.-G.; Kim, Y.D. Toluene oxidation catalyzed by NiO/SiO_2 and $NiO/TiO_2/SiO_2$: Towards development of humidity-resistant catalysts. *Catal. Today* **2016**, *260*, 100–106. [CrossRef]
15. Kim, K.-D.; Nam, J.W.; Seo, H.O.; Kim, Y.D.; Lim, D.C. Oxidation of Toluene on Bare and TiO_2-Covered NiO-$Ni(OH)_2$ Nanoparticles. *J. Phys. Chem. C* **2011**, *115*, 22954–22959. [CrossRef]
16. Jeong, H.; Bae, J.; Han, J.W.; Lee, H. Promoting Effects of Hydrothermal Treatment on the Activity and Durability of Pd/CeO_2 Catalysts for CO Oxidation. *ACS Catal.* **2017**, *7*, 7097–7105. [CrossRef]
17. Dey, S.; Mehta, N.S. Oxidation of carbon monoxide over various nickel oxide catalysts in different conditions: A review. *Chem. Eng. J. Adv.* **2020**, *1*, 100008. [CrossRef]
18. Liu, B.; Ohodnicki, P.R. Fabrication and Application of Single Crystal Fiber: Review and Prospective. *Adv. Mater. Technol.* **2021**, *6*, 2100125. [CrossRef]
19. Fu, Q.; Ai, M.; Duan, Y.; Lu, L.; Tian, X.; Sun, D.; Xu, Y.; Sun, Y. Synthesis of uniform porous NiO nanotetrahedra and their excellent gas-sensing performance toward formaldehyde. *RSC Adv.* **2017**, *7*, 52312–52320. [CrossRef]
20. Ande, C.K.; Knoops, H.C.M.; de Peuter, K.; van Drunen, M.; Elliott, S.D.; Kessels, W.M.M. Role of Surface Termination in Atomic Layer Deposition of Silicon Nitride. *J. Phys. Chem. Lett.* **2015**, *6*, 3610–3614. [CrossRef] [PubMed]
21. Bennett, T.D.; Coudert, F.-X.; James, S.L.; Cooper, A.I. The changing state of porous materials. *Nat. Mater.* **2021**, *20*, 1179–1187. [CrossRef]
22. Mellot-Draznieks, C.; Cheetham, A.K. Encoding evolution of porous solids. *Nat. Chem.* **2016**, *9*, 6–8. [CrossRef] [PubMed]
23. Neagu, D.; Tsekouras, G.; Miller, D.N.; Ménard, H.; Irvine, J.T.S. In situ growth of nanoparticles through control of non-stoichiometry. *Nat. Chem.* **2013**, *5*, 916–923. [CrossRef] [PubMed]
24. Lu, D.; Ouyang, S.; Xu, H.; Li, D.; Zhang, X.; Li, Y.; Ye, J. Designing Au Surface-Modified Nanoporous-Single-Crystalline $SrTiO_3$ to Optimize Diffusion of Surface Plasmon Resonance-Induce Photoelectron toward Enhanced Visible-Light Photoactivity. *ACS Appl. Mater. Interfaces* **2016**, *8*, 9506–9513. [CrossRef] [PubMed]
25. Mo, S.; Li, S.; Li, J.; Deng, Y.; Peng, S.; Chen, J.; Chen, Y. Rich surface Co(iii) ions-enhanced Co nanocatalyst benzene/toluene oxidation performance derived from $Co^{II}Co^{III}$layered double hydroxide. *Nanoscale* **2016**, *8*, 15763–15773. [CrossRef] [PubMed]
26. Xu, H.; Gao, J.; Jiang, D. Stable, crystalline, porous, covalent organic frameworks as a platform for chiral organocatalysts. *Nat. Chem.* **2015**, *7*, 905–912. [CrossRef] [PubMed]
27. Cheng, F.; Lin, G.; Hu, X.; Xi, S.; Xie, K. Porous single-crystalline titanium dioxide at 2 cm scale delivering enhanced photoelectrochemical performance. *Nat. Commun.* **2019**, *10*, 3618. [CrossRef]
28. Tsukada, M.; Adachi, H.; Satoko, C. Theory of Electronic Structure of Oxide Surfaces. *Prog. Surf. Sci.* **1983**, *14*, 113–173. [CrossRef]
29. Liu, B.; Wang, M.; Liu, S.; Zheng, H.; Yang, H. The sensing reaction on the Ni-NiO (111) surface at atomic and molecule level and migration of electron. *Sens. Actuators B Chem.* **2018**, *273*, 794–803. [CrossRef]
30. Afanasev, D.S.; Yakovina, O.A.; Kuznetsova, N.I.; Lisitsyn, A.S. High activity in CO oxidation of Ag nanoparticles supported on fumed silica. *Catal. Commun.* **2012**, *22*, 43–47. [CrossRef]
31. Feng, C.; Liu, X.; Zhu, T.; Tian, M. Catalytic oxidation of CO on noble metal-based catalysts. *Environ. Sci. Pollut. Res.* **2021**, *28*, 24847–24871. [CrossRef] [PubMed]
32. An, A.-F.; Lu, A.-H.; Sun, Q.; Wang, J.; Li, W.-C. Gold nanoparticles stabilized by a flake-like Al_2O_3 support. *Gold Bull.* **2011**, *44*, 217–222. [CrossRef]
33. Allian, A.D.; Takanabe, K.; Fujdala, K.L.; Hao, X.; Truex, T.J.; Cai, J.; Buda, C.; Neurock, M.; Iglesia, E. Chemisorption of CO and Mechanism of CO Oxidation on Supported Platinum Nanoclusters. *J. Am. Chem. Soc.* **2011**, *133*, 4498–4517. [CrossRef] [PubMed]
34. Cao, L.; Liu, W.; Luo, Q.; Yin, R.; Wang, B.; Weissenrieder, J.; Soldemo, M.; Yan, H.; Lin, Y.; Sun, Z.; et al. Atomically dispersed iron hydroxide anchored on Pt for preferential oxidation of CO in H_2. *Nature* **2019**, *565*, 631–635. [CrossRef] [PubMed]
35. An, K.; Alayoglu, S.; Musselwhite, N.; Plamthottam, S.; Melaet, G.; Lindeman, A.E.; Somorjai, G.A. Enhanced CO Oxidation Rates at the Interface of Mesoporous Oxides and Pt Nanoparticles. *J. Am. Chem. Soc.* **2013**, *135*, 16689–16696. [CrossRef] [PubMed]
36. Zhao, J.; Chen, C.; Zhang, B.; Jiao, Z.; Zhang, J.; Yang, J.; Qin, Y. Tuning the selectivity of Pt-catalyzed tandem hydrogenation of nitro compounds via controllable NiO decoration by atomic layer deposition. *Catal. Commun.* **2019**, *121*, 48–52. [CrossRef]
37. Abdullah Mirzaie, R.; Anaraki Firooz, A.; Ghorbani, P. The effect of reaction layer composition on Pt/NiO function for glucose oxidation reaction in neutral media. *Mater. Sci. Eng. C* **2020**, *114*, 111061. [CrossRef]
38. Frati, F.; Hunault, M.O.J.Y.; de Groot, F.M.F. Oxygen K-edge X-ray Absorption Spectra. *Chem. Rev.* **2020**, *120*, 4056–4110. [CrossRef]
39. Zhao, Y.; Chang, C.; Teng, F.; Zhao, Y.; Chen, G.; Shi, R.; Waterhouse, G.I.N.; Huang, W.; Zhang, T. Defect-Engineered Ultrathin δ-MnO_2 Nanosheet Arrays as Bifunctional Electrodes for Efficient Overall Water Splitting. *Adv. Energy Mater.* **2017**, *7*, 1700005. [CrossRef]

40. Chen, J.; Qi, Y.; Lu, M.; Niu, Y.; Zhang, B. Identify fine microstructure of multifarious iron oxides via O K-edge EELS spectra. *Chin. Chem. Lett.* **2022**, *33*, 4375–4379. [CrossRef]
41. Pollak, M.; Gautier, M.; Thromat, N.; Gota, S.; Mackrodt, W.; Saunders, V. An in-situ study of the surface phase transitions of α-Fe_2O_3 by X-ray absorption spectroscopy at the oxygen K edge. *Nucl. Instrum. Methods Phys. Res. Sect. B* **1995**, *97*, 383–386. [CrossRef]
42. Ke, J.; Xiao, J.-W.; Zhu, W.; Liu, H.; Si, R.; Zhang, Y.-W.; Yan, C.-H. Dopant-Induced Modification of Active Site Structure and Surface Bonding Mode for High-Performance Nanocatalysts: CO Oxidation on Capping-free (110)-oriented CeO_2:Ln (Ln = La–Lu) Nanowires. *J. Am. Chem. Soc.* **2013**, *135*, 15191–15200. [CrossRef] [PubMed]
43. Somasundaram, S.; Ill-Min, C.; Vanaraj, R.; Ramaganthan, B.; Mayakrishnan, G. Highly active and reducing agent-free preparation of cost-effective NiO-based carbon nanocomposite and its application in reduction reactions under mild conditions. *J. Ind. Eng. Chem.* **2018**, *60*, 91–101. [CrossRef]
44. Ipsakis, D.; Heracleous, E.; Silvester, L.; Bukur, D.B.; Lemonidou, A.A. Reaction-based kinetic model for the reduction of supported NiO oxygen transfer materials by CH_4. *Catal. Today* **2020**, *343*, 72–79. [CrossRef]
45. Zhang, Q.; Cao, C.; Xu, T.; Sun, M.; Zhang, J.; Wang, Y.; Wan, H. NiO–polyoxometalate nanocomposites as efficient catalysts for the oxidative dehydrogenation of propane and isobutane. *Chem. Commun.* **2009**, *17*, 2376–2378. [CrossRef] [PubMed]
46. Zhai, X.; Liu, C.; Chang, Q.; Zhao, C.; Tan, R.; Peng, H.; Liu, D.; Zhang, P.; Gui, J. TiO_2-nanosheet-assembled microspheres as Pd-catalyst support for highly-stable low-temperature CO oxidation. *New J. Chem.* **2018**, *42*, 18066–18076. [CrossRef]
47. Liu, J.; Ding, T.; Zhang, H.; Li, G.; Cai, J.; Zhao, D.; Tian, Y.; Xian, H.; Bai, X.; Li, X. Engineering surface defects and metal–support interactions on Pt/TiO_2(B) nanobelts to boost the catalytic oxidation of CO. *Catal. Sci. Technol.* **2018**, *8*, 4934–4944. [CrossRef]
48. Jung, C.-H.; Yun, J.; Qadir, K.; Naik, B.; Yun, J.-Y.; Park, J.Y. Catalytic activity of Pt/SiO2 nanocatalysts synthesized via ultrasonic spray pyrolysis process under CO oxidation. *Appl. Catal. B Environ.* **2014**, *154–155*, 171–176. [CrossRef]
49. Zhao, X.; Hu, Y.; Jiang, H.; Yu, J.; Jiang, R.; Li, C. Engineering TiO_2 supported Pt sub-nanoclusters via introducing variable valence Co ion in high-temperature flame for CO oxidation. *Nanoscale* **2018**, *10*, 13384–13392. [CrossRef]
50. Zhang, Y.; Li, Z.; Cao, C.; Hammedi, T.; Waheed, A.; Sami, B.; Zhao, Z.; Li, G. Support Effects on Nickel Hydroxide and Oxide Nanorods Supported Au Nanoparticles for CO Oxidation. *Catal. Lett.* **2023**, 1–11. [CrossRef]
51. Sreethawong, T.; Sitthiwechvijit, N.; Rattanachatchai, A.; Ouraipryvan, P.; Schwank, J.W.; Chavadej, S. Preparation of Au/Y_2O_3 and Au/NiO catalysts by co-precipitation and their oxidation activities. *Mater. Chem. Phys.* **2010**, *126*, 212–219. [CrossRef]
52. Djani, F.; Omari, M.; Martínez-Arias, A. Synthesis, characterization and catalytic properties of La(Ni,Fe)O_3–NiO nanocomposites. *J. Sol-Gel Sci. Technol.* **2015**, *78*, 1–10. [CrossRef]
53. Yi, Y.; Zhang, P.; Qin, Z.; Yu, C.; Li, W.; Qin, Q.; Li, B.; Fan, M.; Liang, X.; Dong, L. Low temperature CO oxidation catalysed by flower-like Ni–Co–O: How physicochemical properties influence catalytic performance. *RSC Adv.* **2018**, *8*, 7110–7122. [CrossRef] [PubMed]
54. Teng, F.; Xu, T.; Zheng, Y.; Liang, S.; Gochoo, B.; Gu, X.; Zong, R.; Yao, W.; Zhu, Y. Formation of hollow NiO single crystals and Ag/NiO flowers. *Mater. Res. Bull.* **2008**, *43*, 3562–3569. [CrossRef]